Electronic Supplementary Material (ESI) for Nanoscale.
This journal is © The Royal Society of Chemistry 2020

ELECTRONIC SUPPLEMENTARY INFORMATION

Nanocage Formation and Structural Anomalies in Imidazolium Ionic Liquid Glasses Governed by Alkyl Chains of Cations

Olga D. Bakulina,[a][b]+ Mikhail Yu. Ivanov,*[a][b]+ Sergey A. Prikhod'ko,[c] Svetlana Pylaeva,[d] Irina V. Zaytseva,[e] Nikolay V. Surovtsev,[e] Nicolay Yu. Adonin,[c] and Matvey V. Fedin*[a][b]

---

[a] *International Tomography Center SB RAS, Institutskaya Street 3a, 630090 Novosibirsk, Russia*
[b] *Novosibirsk State University, Pirogova Street 2, 630090 Novosibirsk, Russia*
[c] *Boreskov Institute of Catalysis SB RAS, Lavrentiev Avenue 5, 630090 Novosibirsk, Russia*
[d] *Universität Paderborn, Warburger Str. 100, 33098 Paderborn, Germany*
[e] *Institute of Automation and Electrometry SB RAS, Koptyug Avenue 1, 630090 Novosibirsk, Russia*
+ These authors contributed equally

Table of Contents

I. Experimental section

Ionic liquids 1-alkyl-3-methylimidazolium tetrafluoroborate ($[C_n mim]BF_4$) with alkyl chains (C_nH_{2n+1}) varying from n=0 to 12 were synthesized according to the procedures described in Ref.[S1] (Scheme 1a). The purity of the obtained compounds was verified using NMR (Section II of ESI). Dibutyl phthalate (DBP) was purchased from Vekton.

The spiro-cyclohexane-substituted nitroxide N1 (14-carbamoyl-7-azadispiro[5.1.5.2]pentadeca-14-ene-7-oxyl) was prepared according to literature protocol.[S2] TEMPO-D_{18} radical ((2,2,6,6-tetramethylpiperidin-1-yl)oxyl) was used as mentioned in the previous study.[S3] The final concentration of spin probe in IL was about 1 mM.

Nitroxide was dissolved in the corresponding IL in concentrations of ~1 mM. Next, the solution was placed in the EPR quartz tube (inner diameter of 2.8 mm), evacuated at 10^{-5} mbar (samples with spiro-cyclohexane-substituted nitroxide radical were simultaneously heated at 85 °C) for 12 hours to reduce the amount of remaining water and to eliminate the remaining oxygen, exposed to 3–5 freeze–pump–thaw cycles, and finally sealed off under vacuum. Samples with TEMPO-D_{18} were prepared in the same way but without heating during pumping to avoid radical reduction.

Pulse EPR measurements were performed using a commercial Bruker Elexsys E580 spectrometer at X-band. The spectrometer was equipped with an Oxford Instruments temperature control system (4−300 K). The echo-detected EPR spectra and transverse relaxation (phase memory) times T_2 were recorded using the standard two-pulse Hahn echo sequence $\pi/2-\tau-\pi-\tau-$echo with pulse lengths 100/50 ns for π and $\pi/2$ pulses. Monoexponential analysis of echo decay vs. 2τ yields the corresponding T_2 value at certain magnetic field. CW EPR spectra were acquired using an X-band Bruker EMX spectrometer (9 GHz). In all experiments the sample was first shock-frozen in liquid nitrogen and then transferred into the cryostat. In this way we ensured that the sample was in glassy state at the beginning of each experiment. The heating/cooling rates were ca. 1 K/min; the sample was equilibrated for at least 10 minutes prior to each EPR measurement. All spectral simulations were done using EasySpin.[S4]

Differential scanning calorimetry (DSC) measurements were performed using a calorimeter DSC-200F3 Maia Netzsch. ILs were loaded into a standard aluminum crucible and cooling (heating) DSC curves were obtained with a rate of 5 K/min. The sharp peaks were attributed to the crystallization (melting) transition, while the glass transition provides a characteristic step-like peculiarity in the DSC curves. The melting temperature was determined from the heating curve to avoid the overcooling effects.

Molecular Dynamics (MD) simulations have been performed in GROMACS simulation package.[S5–S8] OPLS-AA force field[S9] was used for the simulations: IL parameters were taken from Acevedo et al.,[S10,S11] TEMPO parameters were adapted from Sezer et al.[S12] Room temperature simulations for $[C_4mim]BF_4$ solution with TEMPO radical were done for 40 ns after equilibration, then 8 snapshots were extracted from the trajectory every 5 ns. Every snapshot was then annealed to 160 or 190 K in NPT ensemble over a course of 10 ns, followed by NVT production run for 15 ns.

We did not succeed to prepare suitable samples for CW EPR experiments with TEMPO-D_{18} dissolved in [C_0mim]BF_4 and [C_1mim]BF_4. In these two ILs the radical signal was strongly reduced, and it completely disappeared shortly after the sample preparation. IL [C_0mim]BF_4 has a protic nature, and we propose that the radical reduction process takes place in this IL. IL [C_1mim]BF_4 has relatively high melting point, close to 100 °C, therefore it needs to be heated above this temperature to dissolve radical, which causes radical decay during preparation.

II. Synthesis of ionic liquids

Chemicals
Alkyl chlorides, N-methyl imidazole, 1-Ethyl,3-methyl imidazolium chloride, and all standard chemicals were obtained from commercial sources.

Chloride-containing ionic liquids (general procedure)
The ionic liquids C_nH_{2n+1}mimCl (n>2) were obtained by analogy with the literature method[S1] from 1-methyl imidazole and corresponding alkyl chlorides.

1,3-dimethyl imidazolium chloride
1,3-dimethyl imidazolium chloride was obtained by analogy with the literature method.[S13] In a 25 ml glass 4.85 g (59.0 mmol) of imidazole and 5 ml of water were mixed. With stirring, a solution of 5.0 ml of concentrated hydrochloric acid (d 1.18 g/ml, ~11 M, 59.0 mmol) in 5 ml of water was added. At the end of the addition, the acid solution was added dropwise, controlling the pH of the reaction mixture. The addition of acid was completed at a stable pH of reaction mixture of about 3. The mixture was stirred for 1 hr and then water was evaporated in vacuo and product was dried in high vacuum (10^{-3} bar) at 80 °C for 3 hours. The residue was transferred to a glass reactor and 12.0 ml (12.76 g, 141.6 mmol) of dimethyl carbonate was added. The mixture was stirred for 3 hours at 140 °C (the pressure gradually rises to 6 bar). Then the mixture was cooled, the pressure in the reactor was relieved by a tap, the reactor was open and the reaction mixture was transferred to a flask. Volatile components were evaporated in vacuo, a small amount of water and activated carbon were added to the residue. The mixture was stirred for 1 hr and then filtered. Water was evaporated in vacuo and product was dried in high vacuum (10^{-3} bar) at 60 °C for 6 hours. 4.38 g (56 %) of 1,3-dimethyl imidazolium chloride were obtained.

N-methyl imidazolium tetrafluoroborate
A 100 ml round-bottomed flask fitted with magnetic stirrer bar was charged by 6.01 g (73.2 mmol) of N-methyl imidazole and 15 ml of water. With stirring, a solution of 9.9 ml of 7.39 M HBF_4 (d 1.29 g/ml, 73.2 mmol) in 15 ml of water was added. At the end of the addition, the acid solution was added dropwise, controlling the pH of the reaction mixture. The addition of acid was completed at a stable pH of reaction mixture of about 4. The mixture was stirred for 1 hr and then water was evaporated in vacuo and product was dried in high vacuum (10^{-3} bar) at 80 °C for 6 hours. 12.39 g (99 %) of N-methylimidazolium tetrafluoroborate were obtained.

BF_4-containing ionic liquids (general procedure)
A 100 ml round-bottomed flask fitted with magnetic stirrer bar and reflux condenser was charged by 26.5 mmol C_nH_{2n+1}mimCl, 4.39 g (40 mmol) of $NaBF_4$ and 60 ml of acetone. The mixture was stirred for 3 hours at 50 °C. The solid was filtered and washed by 10 ml of acetone. The second portion of $NaBF_4$ (2.18 g, 20 mmol) was added to the filtrate and the resulting mixture was stirred for 3 hours at 50 °C. The solid was filtered and washed by 10 ml of acetone. The filtrate was evaporated in vacuum. The residue was solved in 30 ml of dry dichloromethane (to remove excess of starting salt) and filtered. The filtrate was evaporated and product was dried in high vacuum (10^{-3} bar) at 80 °C for 6 hours. Yield of products are 75-85 %. The reaction of sample of ionic liquid with $AgNO_3$ was negative, that demonstrates the absence of Cl^- ions in the ionic liquid media.

The NMR spectral data of ionic liquids

The NMR spectra were recorded on a Bruker AVANCE 300 spectrometer (^{1}H at 300.13 MHz, ^{19}F at 282.40 MHz) using $CDCl_3$ as solvent (unless otherwise indicated). The chemical shifts are referenced to TMS (^{1}H), CCl_3F (^{19}F, with C_6F_6 as secondary reference (-162.9 ppm)).

N-methylimidazolium tetrafluoroborate ([C_0mim]BF_4)
^{1}H NMR (CD_3CN): δ 12.30 (s, 1H, N-*H*); 8.21 (s, 1H, *H*-2); 7.31 (s, 2H, *H*-4, *H*-5); 3.71 (s, 3H, N-CH_3).
^{19}F NMR (CD_3CN): δ -149.47 (s, 4F, BF_4).

1,3-dimethylimidazolium tetrafluoroborate ([C_1mim]BF_4)
^{1}H NMR: δ 10.56 (s, 1H, *H*-2); 7.78 (s, 2H, *H*-4, *H*-5); 4.05 (s, 6H, N-CH_3).
^{19}F NMR: δ -151.42 (s, 4F, BF_4).

1-Ethyl-3-methylimidazolium tetrafluoroborate ([C_2mim]BF_4)
^{1}H NMR: δ 8.96 (s, 1H, *H*-2); 7.22 (s, 2H, *H*-4, *H*-5); 4.26 (q, 2H, $^{3}J_{HH}$ 7.4 Hz, N-CH_2); 3.96 (s, 3H, N-CH_3); 0.84 (t, 3H, $^{3}J_{HH}$ 7.1 Hz, 2-CH_3).
^{19}F NMR: δ -153.13 (s, 4F, BF_4).

1-Methyl-3-propylimidazolium tetrafluoroborate ([C_3mim]BF_4)
^{1}H NMR: δ 8.71 (s, 1H, *H*-2); 7.27 (s, 2H, *H*-4, *H*-5); 3.99 (t, 2H, $^{3}J_{HH}$ 7.3 Hz, N-CH_2); 3.77 (s, 3H, N-CH_3); 1.84 (qt, 2H, $^{3}J_{HH}$ 7.2 Hz, $^{3}J_{HH}$ 7.3 Hz, 2-CH_2); 0.79 (t, 3H, $^{3}J_{HH}$ 7.4 Hz, 3-CH_3).
^{19}F NMR: δ -152.09 (s, 4F, BF_4).

1-Butyl-3-methylimidazolium tetrafluoroborate ([C_4mim]BF_4)
^{1}H NMR: δ 8.83 (s, 1H, *H*-2); 7.31 (s, 1H, *H*-4); 7.26 (s, 1H, *H*-5); 4.16 (t, 2H, $^{3}J_{HH}$ 7.4 Hz, N-CH_2); 3.94 (s, 3H, NCH_3); 1.84 (tt, 2H, $^{3}J_{HH}$ 7.4 Hz, $^{3}J_{HH}$ 7.4 Hz, 2-CH_2); 1.35 (qt, 2H, $^{3}J_{HH}$ 7.4 Hz, $^{3}J_{HH}$ 7.5 Hz, 3-CH_2); 0.84 (t, 3H, $^{3}J_{HH}$ 7.4 Hz, 4-CH_3).
^{19}F NMR: δ -152.67 (s, 4F, BF_4).

1-Methyl-3-pentylimidazolium tetrafluoroborate ([C_5mim]BF_4)
^{1}H NMR: δ 8.48 (s, 1H, *H*-2); 7.23 (s, 2H, *H*-4, *H*-5); 3.95 (t, 2H, $^{3}J_{HH}$ 7.4 Hz, N-CH_2); 3.71 (s, 3H, N-CH_3); 1.65 (tt, 2H, $^{3}J_{HH}$ 7.1 Hz, $^{3}J_{HH}$ 7.1 Hz, 2-CH_2); 1.01-1.17 (m, 4H, 3,4-CH_2); 0.63 (t, 3H, $^{3}J_{HH}$ 6.8 Hz, 5-CH_3).
^{19}F NMR: δ -151.14 (s, 4F, BF_4).

1-Hexyl-3-methylimidazolium tetrafluoroborate ([C_6mim]BF_4)
^{1}H NMR: δ 8.46 (s, 1H, *H*-2); 7.31 (s, 1H, *H*-4); 7.27 (s, 1H, *H*-5); 4.03 (t, 2H, $^{3}J_{HH}$ 7.3 Hz, N-CH_2); 3.73 (s, 3H, N-CH_3); 1.69 (tt, 2H, $^{3}J_{HH}$ 7.4 Hz, $^{3}J_{HH}$ 7.4 Hz, 2-CH_2); 1.02-1.15 (m, 6H, 3-5-CH_2); 0.60 (t, 3H, $^{3}J_{HH}$ 7.0 Hz, 6-CH_3).
^{19}F NMR: δ -151.38 (s, 4F, BF_4).

1-Heptyl-3-methylimidazolium tetrafluoroborate ([C_7mim]BF_4)
^{1}H NMR: δ 8.56 (s, 1H, *H*-2); 7.29 (s, 1H, *H*-4); 7.27 (s, 1H, *H*-5); 4.01 (t, 2H, $^{3}J_{HH}$ 7.4 Hz, N-CH_2); 3.77 (s, 3H, N-CH_3); 1.71 (tt, 2H, $^{3}J_{HH}$ 7.1 Hz, $^{3}J_{HH}$ 7.0 Hz, 2-CH_2); 0.99-1.26 (m, 8H, 3-6-CH_2); 0.69 (t, 3H, $^{3}J_{HH}$ 6.7 Hz, 7-CH_3).
^{19}F NMR: δ -151.50 (s, 4F, BF_4).

1-Methyl-3-octylimidazolium tetrafluoroborate ([C_8mim]BF_4)
^{1}H NMR: δ 8.66 (s, 1H, *H*-2); 7.33 (s, 1H, *H*-4); 7.29 (s, 1H, *H*-5); 4.11 (t, 2H, $^{3}J_{HH}$ 7.4 Hz, N-CH_2); 3.81 (s, 3H, N-CH_3); 1.79 (tt, 2H, $^{3}J_{HH}$ 7.4 Hz, $^{3}J_{HH}$ 7.4 Hz, 2-CH_2); 1.10-1.26 (m, 10H, 3-7-CH_2); 0.81 (t, 3H, $^{3}J_{HH}$ 6.9 Hz, 7-CH_3).
^{19}F NMR: δ -150.67 (s, 4F, BF_4).

1-Methyl-3-nonylimidazolium tetrafluoroborate ([C_9mim]BF_4)

^{1}H NMR: δ 8.59 (s, 1H, *H*-2); 7.31 (s, 1H, *H*-4); 7.28 (s, 1H, *H*-5); 4.04 (t, 2H, $^3J_{HH}$ 7.4 Hz, N-CH_2); 3.80 (s, 3H, N-CH_3); 1.73 (tt, 2H, $^3J_{HH}$ 6.6 Hz, $^3J_{HH}$ 6.6 Hz, 2-CH_2); 0.99-1.30 (m, 12H, 3-8-CH_2); 0.72 (t, 3H, $^3J_{HH}$ 6.9 Hz, 9-CH_3).

^{19}F NMR: δ -150.98 (s, 4F, BF_4).

1-Decyl-3-methylimidazolium tetrafluoroborate ([C_{10}mim]BF_4)

^{1}H NMR: δ 8.51 (s, 1H, *H*-2); 7.30 (s, 1H, *H*-4); 7.28 (s, 1H, *H*-5); 4.02 (t, 2H, $^3J_{HH}$ 7.5 Hz, N-CH_2); 3.71 (s, 3H, N-CH_3); 1.79 (tt, 2H, $^3J_{HH}$ 7.3 Hz, $^3J_{HH}$ 7.3 Hz, 2-CH_2); 0.89-1.29 (m, 14H, 3-9-CH_2); 0.72 (t, 3H, $^3J_{HH}$ 6.9 Hz, 10-CH_3).

^{19}F NMR: δ -150.55 (s, 4F, BF_4).

1-Methyl-3-undecylimidazolium tetrafluoroborate ([C_{11}mim]BF_4)

^{1}H NMR: δ 8.70 (s, 1H, *H*-2); 7.36 (s, 1H, *H*-4); 7.29 (s, 1H, *H*-5); 4.12 (t, 2H, $^3J_{HH}$ 7.5 Hz, N-CH_2); 3.89 (s, 3H, N-CH_3); 1.82 (tt, 2H, $^3J_{HH}$ 7.3 Hz, $^3J_{HH}$ 7.4 Hz, 2-CH_2); 1.13-1.36 (m, 16H, 3-10-CH_2); 0.83 (t, 3H, $^3J_{HH}$ 6.9 Hz, 11-CH_3).

^{19}F NMR: δ -150.49 (s, 4F, BF_4).

1-Dodecyl-3-methylimidazolium tetrafluoroborate ([C_{12}mim]BF_4)

^{1}H NMR: δ 8.61 (s, 1H, *H*-2); 7.33 (s, 1H, *H*-4); 7.30 (s, 1H, *H*-5); 4.08 (t, 2H, $^3J_{HH}$ 7.4 Hz, N-CH_2); 3.81 (s, 3H, N-CH_3); 1.84 (tt, 2H, $^3J_{HH}$ 7.3 Hz, $^3J_{HH}$ 7.4 Hz, 2-CH_2); 0.88-1.38 (m, 18H, 3-11-CH_2); 0.79 (t, 3H, $^3J_{HH}$ 6.8 Hz, 12-CH_3).

^{19}F NMR: δ -150.41 (s, 4F, BF_4).

III. Molecular dynamics: supplementary details

MD simulations were performed in GROMACS simulation package. We have used PME[S14] to of the 6-th order to evaluate Coulomb interactions. We have used LINCS algorithm to constrain H-bonds.[S15] Velocity rescaling thermostat[S16] was used for all simulations, Berendsen barostat was used during NPT annealing. Temperature annealing to 190 K and 160 K was performed independently for snapshots extracted from the room temperature trajectory.

Figure S1 shows the distribution of nonpolar clusters' sizes, butyl tails were attributed to a cluster as long as distance between any of three last carbon atoms of the butyl chain was smaller than 0.38 nm. Interestingly, the mean size of the cluster depends monotonically on temperature being the largest at 160 K and then gradually decreasing at 190 and 298 K. We think that this trend is responsible for the growth of the mobile fraction of radicals with temperature manifested by $M(T)$ curves: partitioning of larger clusters leads to 'exclusion' of radicals from nonpolar domains. This trend also agrees with the data of Figure 5, which show a decrease of $g_{\mathrm{Bu}}(r)$ with temperature at r~0.5-1 nm (~cluster size, Fig.4). Therefore, though indirectly, MD data agrees with the proposal that structural anomalies sensed by radical probes are inherent to all nonpolar domains of IL. Likely, a crystallization-like behavior occurs inside the nonpolar nano-domains, and those of them which include radical impose more rigid environment on it leading to a suppression of molecular librations. The latter, reasonably, is manifested in anomalous decrease of $L(T)$ with temperature between T_{an} and T_{g}.

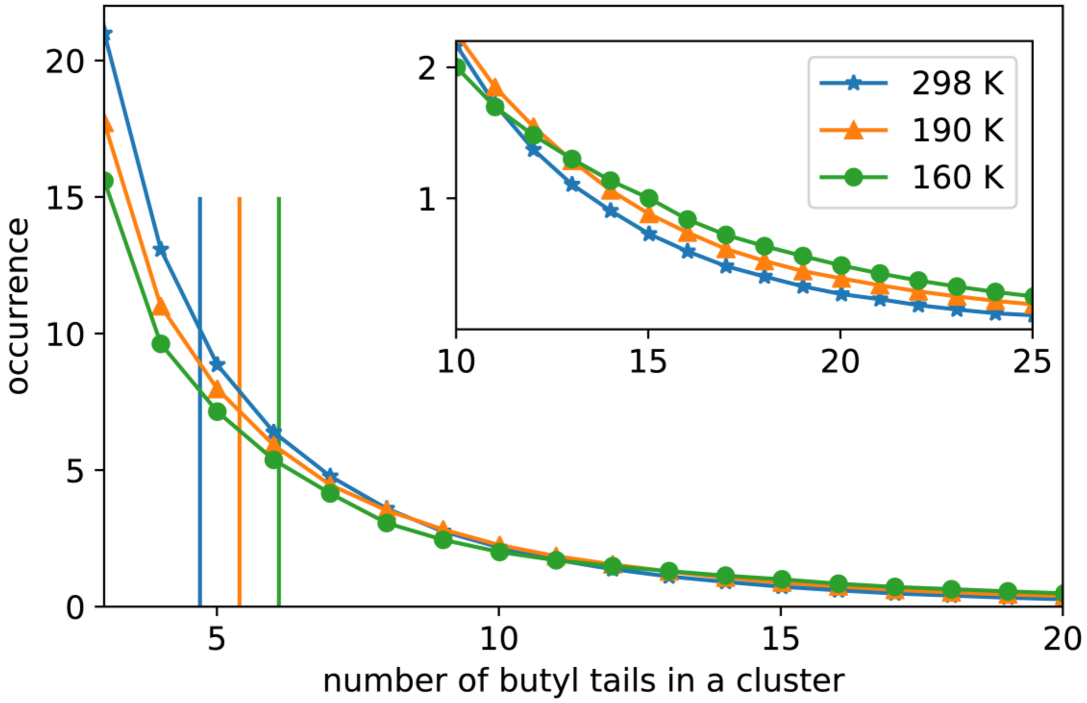

Figure S1. Distribution of nonpolar cluster sizes vs. the number of butyl tails in the cluster for $[C_4mim]BF_4$ at 160-298 K (indicated). The vertical lines show the average size of the cluster, which equals 6.1, 5.4 and 4.7 butyl tails per cluster at 160, 190 and 298 K, respectively.

IV. Differential scanning calorimetry (DSC) measurements

DSC measurements were performed using DSC 200 F3 Maia (NETZSCH) equipment. Samples were placed in the closed and pressed alumina melting pot with 25 μl volume. Setup calibration was done using indium (99,999 %) and zinc (99 %) purchased from Sigma Aldrich. DSC curves were measured on a cooling and heating in temperature range from -140 to 120 ^{o}C with the rate 5 K/min.

All measurements were done in helium atmosphere. Data analysis was made according to the procedure described in the literature.[S17] Measured glass transition temperatures and the comparison with the literature data are listed in the Table S1.

Table S1. Glass transition temperatures of studied ILs determined by DSC.

Ionic liquid	T_g[a] / K	T_g[b] / K
[C_0mim]BF_4	no T_g	no data
[C_1mim]BF_4	no T_g	no data
[C_2mim]BF_4	167.9	186.15[S18] 180.15[S19] 184[S20] 183.75[S21] 181.15[S22] 178[S23]
[C_3mim]BF_4	174.6	185.15[S22] 259.25[S24]
[C_4mim]BF_4	187.7*	188.15[S22] 202[S24] 176.15[S25] 188.85[S26] 185.85[S27]
[C_5mim]BF_4	181.3	185.65[S24] 185.75[S27]
[C_6mim]BF_4	188	190.75[S24] 187.55[S27] 194[S28]
[C_7mim]BF_4	186.6	192.75[S24] 187.15[S27]
[C_8mim]BF_4	188.8	194.65[S24] 187.25[S27] 192[S28]
[C_9mim]BF_4	190.4	195.95[S24]
[C_{10}mim]BF_4	236	no data
[C_{11}mim]BF_4	no T_g	no data
[C_{12}mim]BF_4	no T_g	no data
dibutyl phthalate	177.8	174.35[S29]

[a] This work, (*)[S30]. [b] Literature data.

V. EPR of stochastic molecular librations

EPR is a very useful tool to investigate the mobility of paramagnetic molecules in various media. In particular, stochastic molecular librations of molecules commonly occur in molecular glasses. They represent the small-angle wobbling of molecules driven by thermal energy. When spin probe, most often the nitroxide radical, is placed in glass, it exhibits similar librations to those occurring in the surrounding matrix. In other words, being tightly embedded in the glass, the spin probe follows its molecular mobility/wobbling. This makes spin probes in the glasses true reporters of the state of the surrounding matrix.

EPR is generally sensitive to the mobility of the nitroxide probe. Most commonly, the shape of CW EPR spectrum allows one to determine the rotational correlation times of the nitroxide (see Section VII of ESI, for example). However, when the mobility is restricted to small-angle wobbling (e.g. $<1^{o}$), CW EPR becomes insensitive. At the same time, pulse EPR based relaxation methods come into play, because the electron spin relaxation is decently influenced even by such small motions as librations.

A series of works by Dzuba et.al. developed a potent approach to characterize the librations of nitroxide probes in molecular glasses.[S31,S32] In fact, the product $<\alpha^2>\tau_c$ can be experimentally obtained, where $<\alpha^2>$ is the mean square angular amplitude of motion and τ_c is the corresponding correlation time. This approach is based on the measurements of transverse relaxation times (T_2) of nitroxide in two definite spectral positions.

The theoretical consideration of spin relaxation induced by the fast (sub-microsecond) stochastic molecular librations predicts the exponential decay of the two-pulse electron spin echo (ESE) signal upon incrementing the time delay between two pulses. The decay rate is determined by spectral anisotropy at the position of the nitroxide spectrum (positions **I** and **II** in Fig.S2a). The nitroxide spectrum is split into three lines due to the hyperfine interaction (HFI) between the spin of unpaired electron and the spin of nitrogen nucleus (I=1). The central component (**I**) is influenced mainly by the anisotropy of the g-tensor, with the anisotropy of HFI being negligible; therefore, it possesses the smallest anisotropy and the narrowest linewidth. For the broadest high-field component (**II**), both the anisotropies influence the spectral shape in an additive way, so it is the most anisotropic and the broadest one. Therefore, the decay rates for the field positions (**I**) and (**II**) are essentially different. However, there are other additive relaxation mechanisms contributing to the resulting T_2 values. Therefore, in order to elucidate pure libration-induced relaxation, one should subtract the relaxation rates (inverse relaxation times T_2) in the two spectral positions (**I**) and (**II**), as is illustrated in Fig.S2a.

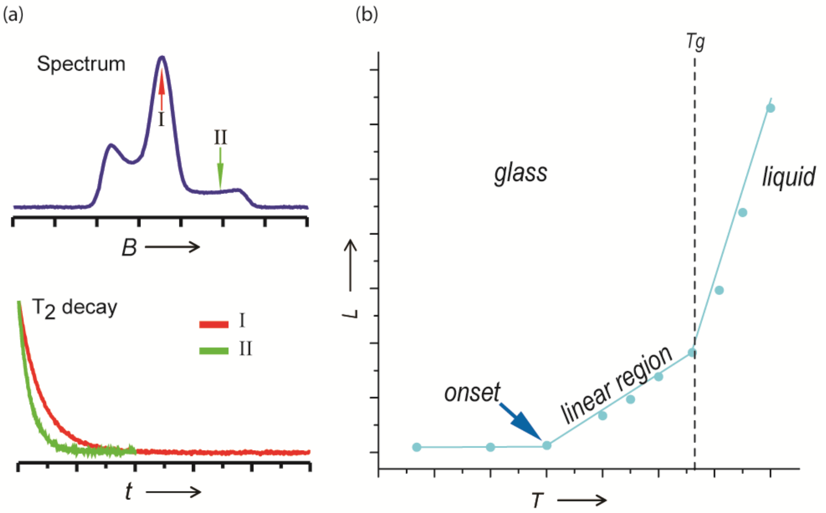

Figure S2. Sketch of the pulse EPR analysis scheme. (a) Two-pulse electron spin echo detected spectrum (top). The T_2 decay is measured by incrementing τ delay in $\pi/2$ - τ - π - echo sequence at two spectral positions **I** and **II**. Corresponding T_2 times are obtained by monoexponential analysis. (b) Typical $L(T)$ dependence showing low-temperature region of no librations, then their onset, linear region of effective librations, and, finally, transition into a liquid state with steep increase of molecular motion.

As a result, we obtain pure libration-based contribution, which we denoted $L \equiv (1/T_2^{II} - 1/T_2^{I})$. Redfield relaxation theory shows that for fast (sub-microsecond) and small-angle librations $L \approx C \langle \alpha^2 \rangle \tau_c$, where $\langle \alpha^2 \rangle$ and τ_c were defined above, and C is the numerical coefficient, whose value was semi-empirically determined to be $9 \cdot 10^{16}$ s^{-2} for nitroxide radicals.[S32]

However, not the absolute value of L at certain temperature, but the shape of the $L(T)$ dependence is most informative and has to be analyzed. Theory of atomic displacements predicts that $L(T)$ should linearly grow with temperature. Figure S2b sketches possible behaviors of $L(T)$ dependence. The onset of librations indicates the temperature where librations start to influence electron spin relaxation strong enough to be detected in ESE-based T_2 measurements. The slope of the $L(T)$ curve characterizes the intensity of librations. When glass softens and transforms into a liquid, the amplitude of the nitroxide motions drastically grows, leading to a steep rise of $L(T)$ until T_2 becomes too short to be measured. Thus, in general, no other behaviors are to be expected for the $L(T)$, unless some structural rearrangements occur. There is no reason for $L(T)$ curve to change from a rising trend to a decrease as T increases, because kT driving librations does grow. Thus, any deviations from monotonic linear growth indicate some structural changes in the glassy matrix surrounding the nitroxide.

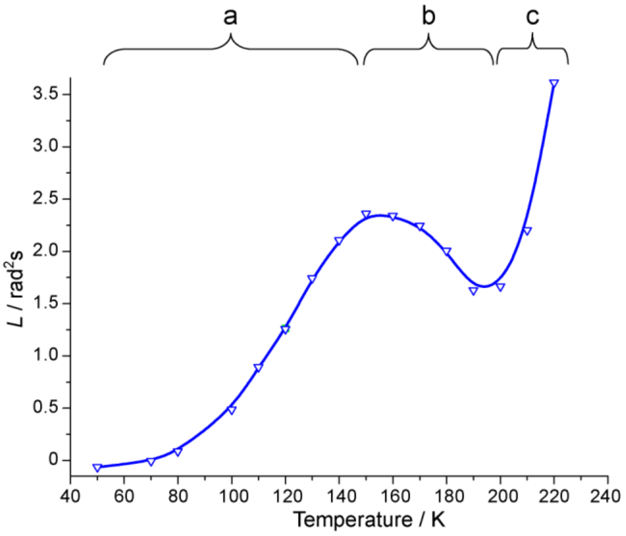

Figure S3. Representative schematic temperature dependence of the motional parameter L for nitroxide radical in ILs {a}, {b} and {c} indicate the motional regimes, see text for details. {b} is the region of anomaly.

However in the studied ILs $L(T)$ curve has three characteristic regions, that are marked as {a}, {b} and {c} in Figure S3. The rise of $L(T)$ function at ~70 K (region {a}) indicates the onset of stochastic molecular librations in IL. Further increase of the stochastic librations amplitude [growth of $L(T)$] is observed up to ~140 K (region {a} in Fig.S3). However, then the anomalous suppression of the stochastic librations is found within ~140−200 K (region {b}), which has never been observed in common organic glasses or biological membranes. At even higher temperatures T > 200 K, which are close to T_g of the studied ILs, the trend reverts to the rise again (region {c}), to be assigned to the unlocking of diffusive rotation of the radical in softened/melted IL. The linear growth of $L(T)$ in region {a} is a typical behavior, that was observed previously in various organic glasses and biological membranes. The nonlinear region {b} of $L(T)$ is the most interesting and represents the structural rearrangements in bulk IL. It was noticed that the position of local minimum of $L(T)$ curve clearly coincides with the T_g temperature of given IL.

VI. Temperature dependence of T_2 relaxation time

Figure S4 reports the data on the basis of which the *L*(*T*) curves were calculated for each case. It shows the echo-detected EPR spectrum with two characteristic spectral positions **I** and **II** (Fig. S4a), individual T_2 measured at **I** and **II** positions for each IL, and their difference.

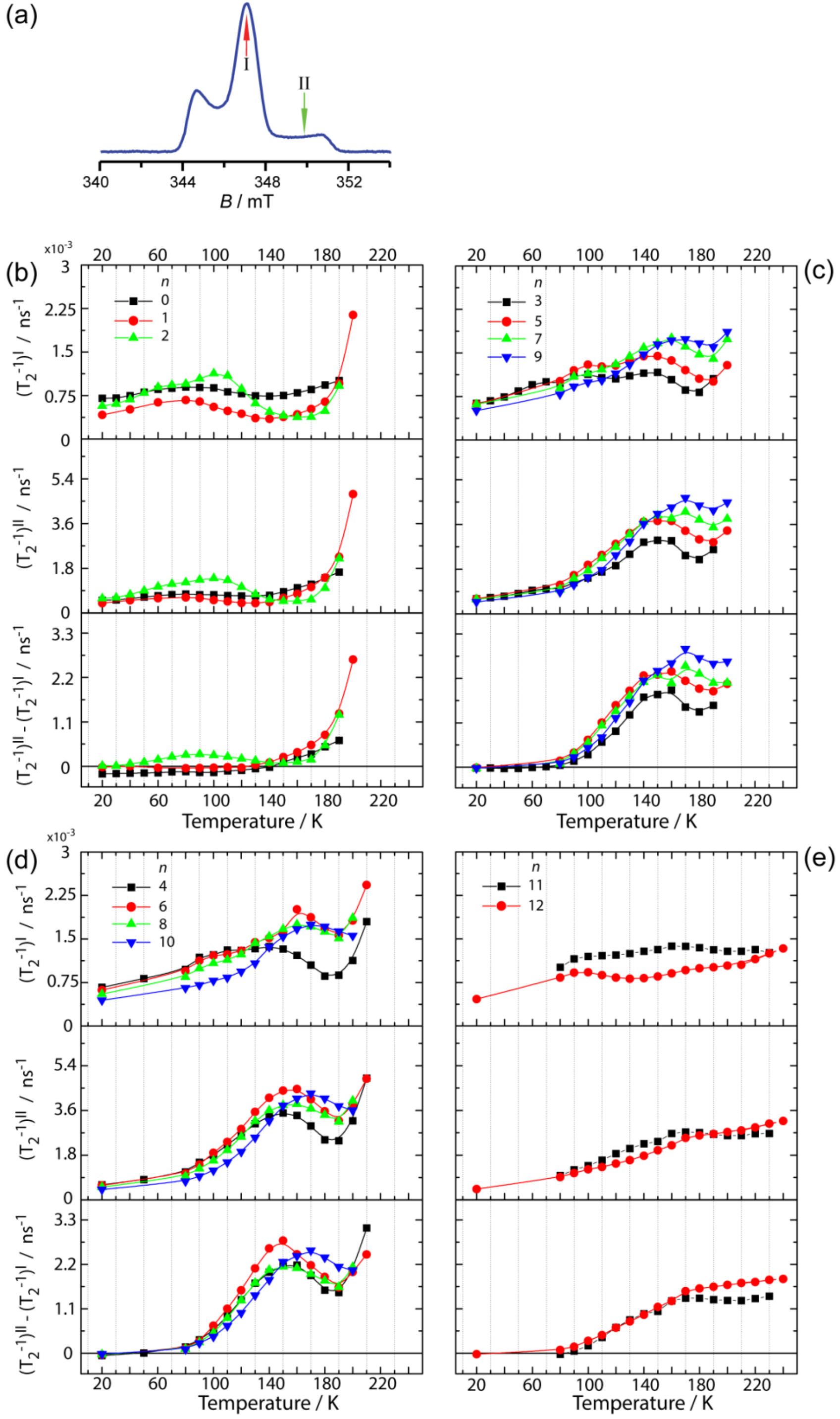

Figure S4. (a) Illustrative echo-detected spectrum with indicated field positions where T_2 was measured. (b)-(e) Temperature dependence of T_2^{-1} measured at low (**I** at Fig. S4a), high (**II** at Fig. S4a) field positions and their difference for all presented solvents. Lines represent the splines guiding the eye.

It is evident that the difference of inverse T_2 values (proportional to *L*) for [C$_0$mim]BF$_4$ and [C$_1$mim]BF$_4$ is negative in the temperature range 20 – 130 K (Figure S4b), but in the final Figure 1 (main text) *L* values are biased to a zero level at low temperatures. The negative *L* depicts the domination of nuclear spin diffusion processes when librations are negligible.[S33] This mechanism is caused by additional stochastic interaction between unpaired electron of the radical with nuclear spins of the protons in surrounding medium. The shape of the echo-detected spectrum (Figure S4a) indicates that the number of detected radical spins in field position (orientation) **I** is much higher compared to that in orientation **II** – as is reflected in their relative signal intensities. In other words, microwave pulses applied at field position **I** excite more electron spins compared to position **II**; therefore, flip-flop processes with nuclear spins are more pronounced in position **I** and shorter T_2 relaxation time is obtained in this field position at low-temperature limit. As a result, L parameter gets the negative value.

It is well known that spin diffusion process is temperature independent. At low temperatures radical libration mechanism is suppressed, and spin diffusion process plays the dominant role and determines the obtained relaxation times. As the temperature is increased, the libration-induced relaxation takes over the spin diffusion, and L becomes positive. Therefore, the negative L value at low temperatures (50 K and lower) can be considered as a constant background level. We subtract it for proper analysis of $L(T)$ dependence. For ILs with $n>1$ L value is positive even at low temperatures, correlating with higher local density of solvent protons around spin probe due to the longer alkyl chains.

VII. Continuous wave EPR spectra

Figures S5-S8 show the CW EPR spectra of spin probe TEMPO-D_{18} dissolved in the corresponding ILs. The computer simulations were performed using EasySpin software.[S4] Spectral parameters used in simulations are listed in the Tables S2-S11.

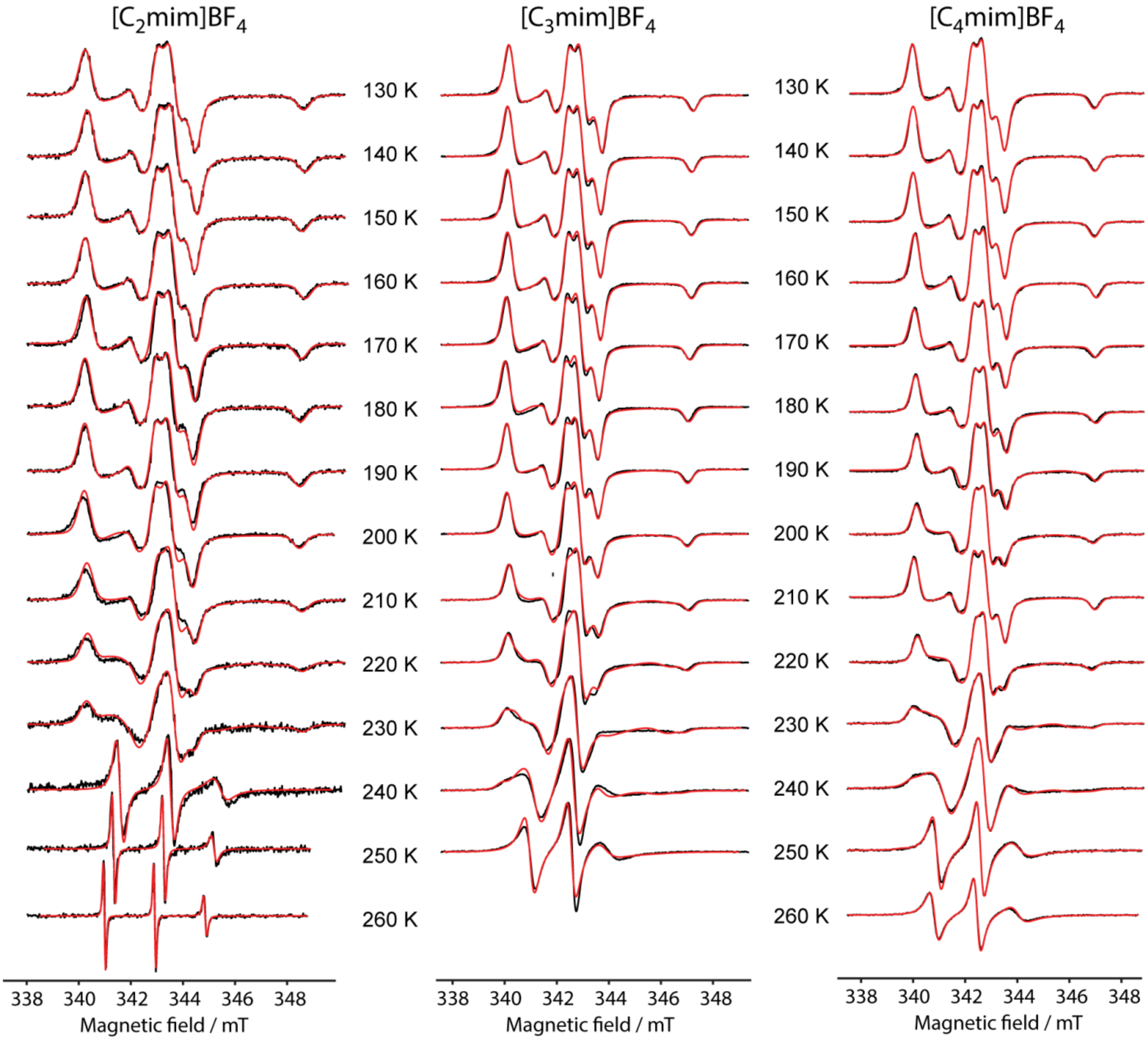

Figure S5. CW EPR spectra of TEMPO-D_{18} dissolved in the [C_2mim]BF_4, [C_3mim]BF_4 and [C_4mim]BF_4 vs. temperature. Black lines represent the experimental data, red ones - the simulation results.

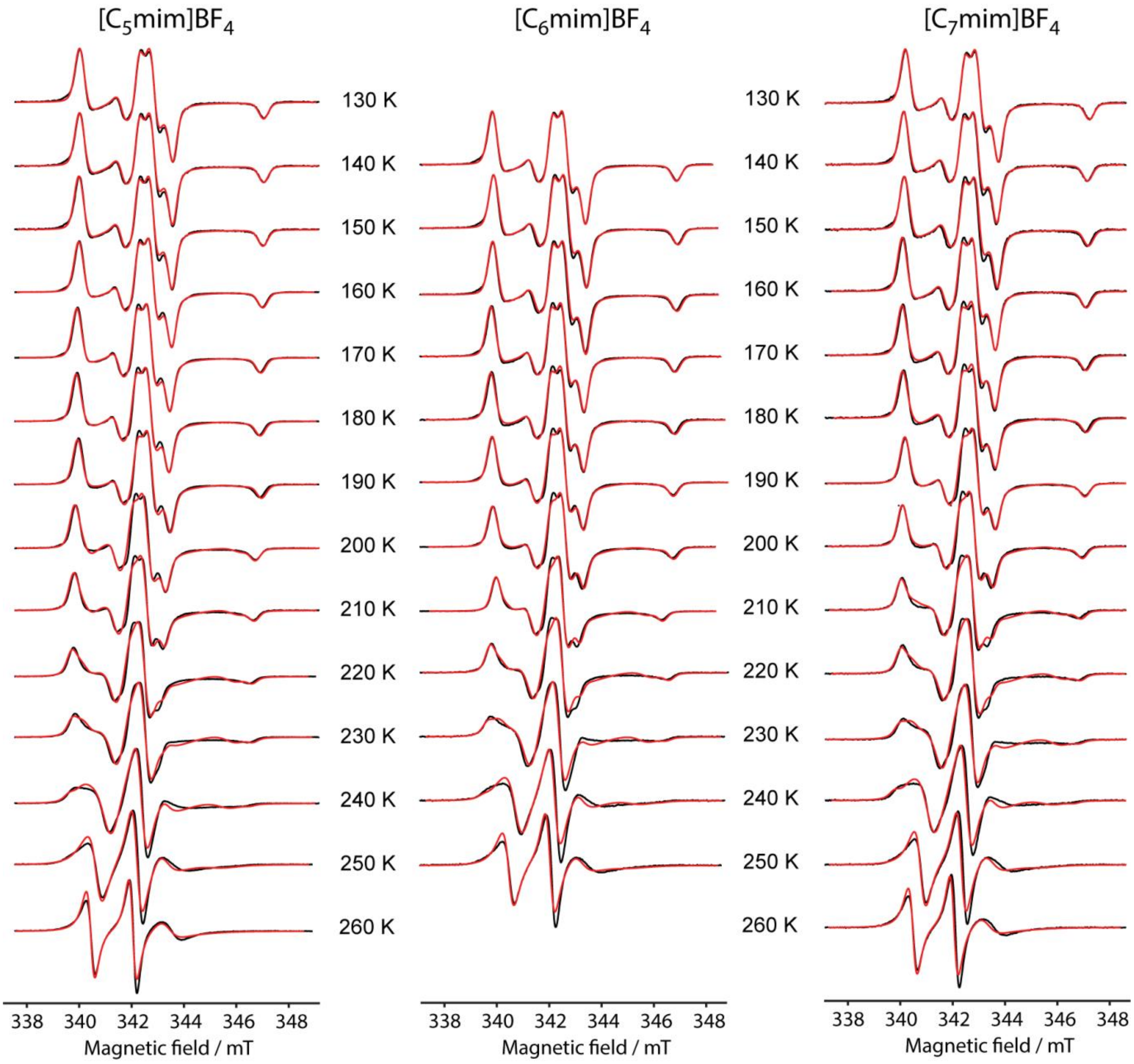

Figure S6. CW EPR spectra of TEMPO-D$_{18}$ dissolved in the [C$_5$mim]BF$_4$, [C$_6$mim]BF$_4$ and [C$_7$mim]BF$_4$ vs. temperature. Black lines represent the experimental data, red ones - the simulation results.

Figure S7. CW EPR spectra of TEMPO-D_{18} dissolved in the [C_8mim]BF_4, [C_9mim]BF_4 and [C_{10}mim]BF_4 vs. temperature. Black lines represent the experimental data, red ones - the simulation results.

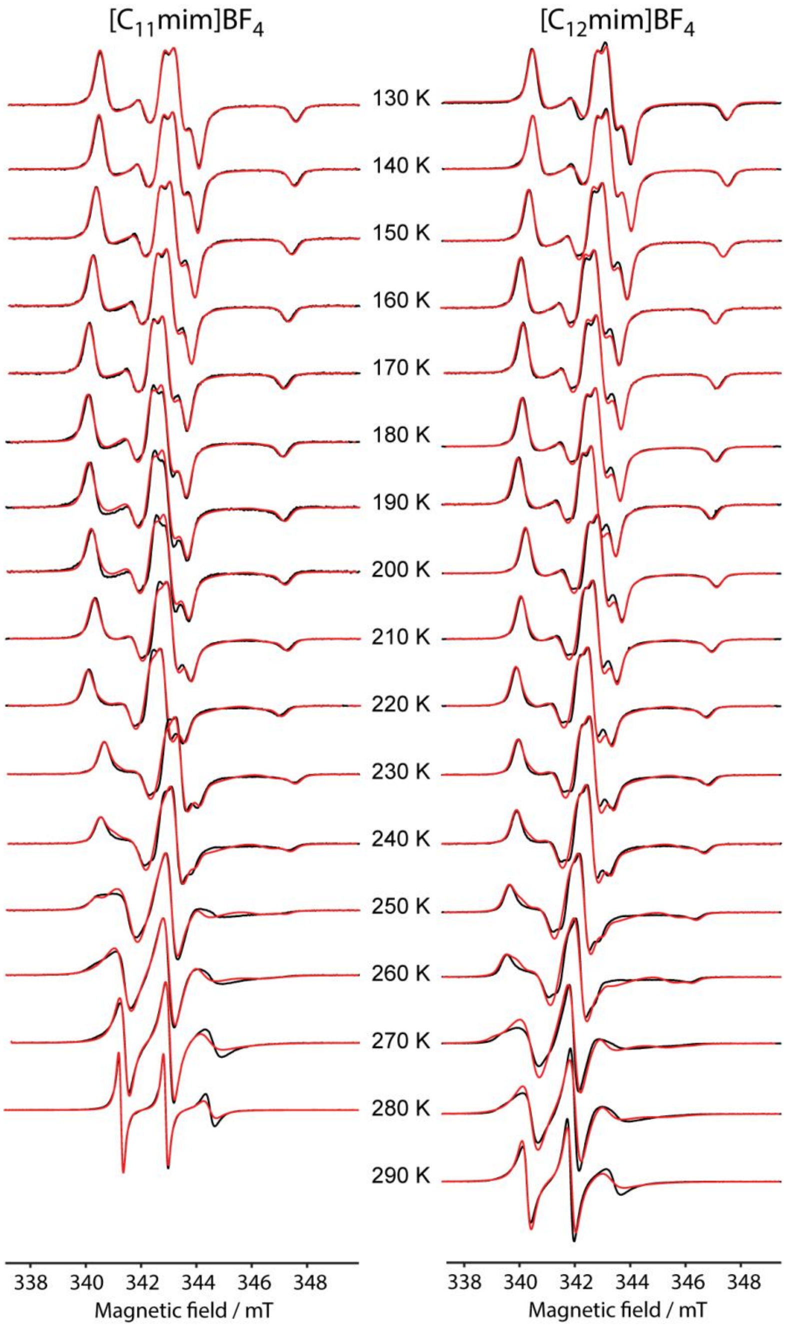

Figure S8. CW EPR spectra of TEMPO-D_{18} dissolved in the [C_{11}mim]BF_4 and [C_{12}mim]BF_4 vs. temperature. Black lines represent the experimental data, red ones - the simulation results.

Table S2. List of parameters used in simulation of CW EPR spectra of TEMPO-D$_{18}$ in [C$_2$mim]BF$_4$.

		Mobile fraction			Immobile fraction		
T / K	M	τ_c / ns	g-tensor	A-tensor / MHz	g-tensor	A-tensor / MHz	Astrain / MHz
100	0	-	[2.0112 2.0077 2.0038]	[18.3 19.8 100.6]	[2.0112 2.0077 2.0038]	[18.3 19.8 100.6]	[4.3 0 7.9]
110	0	-					
120	0	-					
130	0	-					
140	0	-					
150	0	-					
160	0	-					
170	0	-		[18.3 19.8 99.5]		[18.3 19.8 99.5]	
180	0	-					
190	0	-					
200	0.09	3.7					
210	0.29	6.5					
220	0.47	5.5					
230	0.60	5.1					
240	1	1.2		[18.3 19.8 102.0]		[18.3 19.8 102.0]	
250	1	0.5					
260	1	0.2					

Table S3. List of parameters used in simulation of CW EPR spectra of TEMPO-D$_{18}$ in [C$_3$mim]BF$_4$.

		Mobile fraction			Immobile fraction		
T / K	M	τ_c / ns	g-tensor	A-tensor / MHz	g-tensor	A-tensor / MHz	Astrain / MHz
130	0	-	[2.0112 2.0077 2.0037]	[17.7 19.7 99.3]	[2.0112 2.0077 2.0037]	[17.7 19.7 99.3]	[2.9 0 6.2]
140	0	-					
150	0	-					
160	0	-					
170	0.06	3.7					
180	0.1	3.7					
190	0.16	6.1		[17.7 19.7 97.6]		[17.7 19.7 97.6]	
200	0.26	7.2					
210	0.41	7.5					
220	0.59	8.2					
230	0.82	7.7					
240	0.93	4.6					
250	1	2.7		[17.7 19.7 100.7]		[17.7 19.7 100.7]	

Table S4. List of parameters used in simulation of CW EPR spectra of TEMPO-D$_{18}$ in [C$_5$mim]BF$_4$.

		Mobile fraction			Immobile fraction		
T / K	M	τ_c / ns	g-tensor	A-tensor / MHz	g-tensor	A-tensor / MHz	Astrain / MHz
130	0	-	[2.0113 2.0078 2.0038]	[17.9 19.7 98.8]	[2.0113 2.0078 2.0038]	[17.9 19.7 98.8]	[4.3 0 6]
140	0	-					
150	0	-					

160	0.08	6.1					
170	0.11	6.6					
180	0.17	9.4					
190	0.22	7.2					
200	0.35	12.3		[17.9 19.7 97.1]		[17.9 19.7 97.1]	
210	0.47	10.1					
220	0.69	8.5					
230	0.806	7.7					
240	0.93	5.7					
250	1	3.7		[17.9 19.7 100.5]		[17.9 19.7 100.5]	
260	1	2.4					

Table S5. List of parameters used in simulation of CW EPR spectra of TEMPO-D_{18} in $[C_6mim]BF_4$.

			Mobile fraction		Immobile fraction		
T / K	M	τ_c / ns	g-tensor	A-tensor / MHz	g-tensor	A-tensor / MHz	Astrain / MHz
140	0	-	[2.0112 2.0077 2.0037]	[18.2 19.7 98.7]	[2.0112 2.0077 2.0037]	[18.2 19.7 98.7]	[5.4 0 6.2]
150	0	-					
160	0	-					
170	0.08	6.6					
180	0.16	7.9					
190	0.23	7.8		[18.2 19.7 97.2]		[18.2 19.7 97.2]	
200	0.33	7.6					
210	0.50	8.1					
220	0.65	8.3		[18.2 19.7 96]		[18.2 19.7 96]	
230	0.86	7.0					
240	0.96	4.8					
250	1	3.0		[18.2 19.7 99.3]		[18.2 19.7 99.3]	

Table S6. List of parameters used in simulation of CW EPR spectra of TEMPO-D_{18} in $[C_7mim]BF_4$.

		Mobile fraction			Immobile fraction		
T / K	M	τ_c / ns	g-tensor	A-tensor / MHz	g-tensor	A-tensor / MHz	Astrain / MHz
130	0	-	[2.0113 2.0077 2.0037]	[17.9 19.7 98.7]	[2.0113 2.0077 2.0037]	[17.9 19.7 98.7]	[4.6 0 5.9]
140	0	-					
150	0	-					
160	0	-					
170	0.13	9.9					
180	0.21	11.1					
190	0.26	8.9		[17.9 19.7 96.7]		[17.9 19.7 96.7]	
200	0.36	7.7					
210	0.58	7.2					
220	0.71	7.9					
230	0.86	7.0					
240	0.91	5.1					
250	1	3.4		[17.9 19.7 97.6]		[17.9 19.7 97.6]	
260	1	2.7					

Table S7. List of parameters used in simulation of CW EPR spectra of TEMPO-D_{18} in $[C_8mim]BF_4$.

		Mobile fraction			Immobile fraction		
T / K	M	τ_c / ns	g-tensor	A-tensor / MHz	g-tensor	A-tensor / MHz	Astrain / MHz
100	0	-	[2.0112 2.0076 2.0036]	[18.2 20.3 99.5]	[2.0112 2.0076 2.0036]	[18.2 20.3 99.5]	[5.3 2.2 8.4]
110	0	-					
120	0	-					
130	0	-					
140	0	-		[18.2 20.3 98.6]		[18.2 20.3 98.6]	
150	0	-					
160	0	-					
170	0.07	4.5					
180	0.16	4.6					
190	0.22	6.7					
200	0.33	6.9		[18.2 20.3 96.9]		[18.2 20.3 96.9]	
210	0.50	7.8					
220	0.68	7.6					
230	0.87	6.6					
240	0.93	4.6					
250	0.99	3.6					
260	1	2.1		[18.2 20.3 101]		[18.2 20.3 101]	
270	1	1.5					
280	1	0.9					
290	1	0.6		[18.2 20.3 98.6]		[18.2 20.3 98.6]	

Table S8. List of parameters used in simulation of CW EPR spectra of TEMPO-D_{18} in $[C_9mim]BF_4$.

		Mobile fraction			Immobile fraction		
T / K	M	τ_c / ns	g-tensor	A-tensor / MHz	g-tensor	A-tensor / MHz	Astrain / MHz
100	0	-	[2.0112 2.0076 2.0036]	[17.9 20 99]	[2.0112 2.0076 2.0036]	[17.9 20 99]	[4.8 0 7]
110	0	-					
120	0	-					
130	0	-					
140	0	-					
150	0	-					
160	0	-					
170	0.08	6.8		[17.9 20 97.6]		[17.9 20 97.6]	
180	0.17	7.7					
190	0.29	8.9					
200	0.39	7.5		[17.9 20 96.3]		[17.9 20 96.3]	
210	0.55	7.9					
220	0.731604	6.3					
230	0.85	5.4					
240	0.89	4.3		[17.9 20 99.6]		[17.9 20 99.6]	
250	1	3.1		[17.9 20 100.9]		[17.9 20 100.9]	
260	1	2.6		[17.9 20 100.6]		[17.9 20 100.6]	

Table S9. List of parameters used in simulation of CW EPR spectra of TEMPO-D_{18} in $[C_{10}mim]BF_4$.

		Mobile fraction			Immobile fraction		
T / K	M	τ_c / ns	g-tensor	A-tensor / MHz	g-tensor	A-tensor / MHz	Astrain / MHz
140	0	-	[2.0112 2.0077 2.0037]	[18.7 19.7 98.5]	[2.0112 2.0077 2.0037]	[18.7 19.7 98.5]	[5.8 0.9 6.6]
150	0	-					
160	0.08	4.8					
170	0.1	58					
180	0.14	5.6					
190	0.23	6.7		[18.7 19.7 97.2]		[18.7 19.7 97.2]	
200	0.28	8.1					
210	0.43	7.9					
220	0.61	7.8					
230	0.67	7.6		[18.7 19.7 95.8]		[18.7 19.7 95.8]	
240	0.82	5.8					
250	0.89	5.5					
260	1	2.5		[18.7 19.7 100.9]		[18.7 19.7 100.9]	
270	1	1.6		[18.7 19.7 100.5]		[18.7 19.7 100.5]	

Table S10. List of parameters used in simulation of CW EPR spectra of TEMPO-D_{18} in $[C_{11}mim]BF_4$

		Mobile fraction			Immobile fraction		
T / K	M	τ_c / ns	g-tensor	A-tensor / MHz	g-tensor	A-tensor / MHz	Astrain / MHz
120	0	-	[2.0111 2.0077 2.0037]	[18.4 19.7 99]	[2.0111 2.0077 2.0037]	[18.4 19.7 99]	[5.8 4.2 7.1]
130	0	-					
140	0	-					
150	0	-					
160	0.06	4.3					
170	0.12	11.4					
180	0.17	10.5					
190	0.23	9.2					
200	0.29	8.5		[18.4 19.7 98]		[18.4 19.7 98]	
210	0.36	8.1					
220	0.46	7.5					
230	0.53	7.3		[18.4 19.7 96.6]		[18.4 19.7 96.6]	
240	0.65	7.1					
250	0.87	5					
260	1	3.6		[18.4 19.7 104.7]		[18.4 19.7 104.7]	
270	1	2.5		[18.4 19.7 101.7]		[18.4 19.7 101.7]	
280	1	1.3		[18.4 19.7 99]		[18.4 19.7 99]	

Table S11. List of parameters used in simulation of CW EPR spectra of TEMPO-D_{18} in $[C_{12}mim]BF_4$

		Mobile fraction			Immobile fraction		
T / K	M	τ_c / ns	g-tensor	A-tensor / MHz	g-tensor	A-tensor / MHz	Astrain / MHz

120	0	-	[2.0111 2.0076 2.0037]	[17.9 19.7 99.1]	[2.0111 2.00762.0037]	[17.9 19.7 99.1]	[8.3 0 6.5]
130	0	-					
140	0	-					
150	0.07	3					
160	0.1	8.1					
170	0.13	8.					
180	0.17	9					
190	0.22	9.2					
200	0.26	8.9		[17.9 19.7 97.3]		[17.9 19.7 97.3]	
210	0.32	8.5					
220	0.40	8.3					
230	0.48	8					
240	0.572	7.9		[17.9 19.7 95.7]		[17.9 19.7 95.7]	
250	0.67	7.7					
260	0.78	7.7					
270	0.96	4.3		[17.9 19.7 101.1]		[17.9 19.7 101.1]	
280	1	3.5		[17.9 19.7 102.9]		[17.9 19.7 102.9]	
290	1	2.3		[17.9 19.7 101.7]		[17.9 19.7 101.7]	

References

S1 J. Dupont, C. S. Consorti, P. a. Z. Suarez and R. F. De Souza, Preparation of 1-butyl-3-methyl imidazolium-based room temperature ionic liquids, *Org. Synth.*, 2002, **79**, 236.

S2 I. A. Kirilyuk, Y. F. Polienko, O. A. Krumkacheva, R. K. Strizhakov, Y. V. Gatilov, I. A. Grigor'ev and E. G. Bagryanskaya, Synthesis of 2,5-bis(spirocyclohexane)-substituted nitroxides of pyrroline and pyrrolidine series, including thiol-specific spin label: An analogue of MTSSL with long relaxation time, *J. Org. Chem.*, 2012, **77**, 8016–8027.

S3 M. Y. Ivanov, S. A. Prikhod'ko, N. Y. Adonin, I. A. Kirilyuk, S. V. Adichtchev, N. V. Surovtsev, S. A. Dzuba and M. V. Fedin, Structural Anomalies in Ionic Liquids near the Glass Transition Revealed by Pulse EPR, *J. Phys. Chem. Lett.*, 2018, **9**, 4607–4612.

S4 S. Stoll and A. Schweiger, EasySpin, a comprehensive software package for spectral simulation and analysis in EPR, *J. Magn. Reson.*, 2006, **178**, 42–55.

S5 M. J. Abraham, T. Murtola, R. Schulz, S. Páll, J. C. Smith, B. Hess and E. Lindah, Gromacs: High performance molecular simulations through multi-level parallelism from laptops to supercomputers, *SoftwareX*, 2015, **1**–**2**, 19–25.

S6 D. Van Der Spoel, E. Lindahl, B. Hess, G. Groenhof, A. E. Mark and H. J. C. Berendsen, GROMACS: Fast, flexible, and free, *J. Comput. Chem.*, 2005, **26**, 1701–1718.

S7 H. J. C. Berendsen, D. van der Spoel and R. van Drunen, GROMACS: A message-passing parallel molecular dynamics implementation, *Comput. Phys. Commun.*, 1995, **91**, 43–56.

S8 Lindahl, Abraham, Hess and van der Spoel, GROMACS 2020.1 Source code, , DOI:10.5281/ZENODO.3685919.

S9 M. J. Robertson, J. Tirado-Rives and W. L. Jorgensen, Improved Peptide and Protein Torsional Energetics with the OPLS-AA Force Field, *J. Chem. Theory Comput.*, 2015, **11**, 3499–3509.

S10 B. Doherty, X. Zhong, S. Gathiaka, B. Li and O. Acevedo, Revisiting OPLS Force Field Parameters for Ionic Liquid Simulations, *J. Chem. Theory Comput.*, 2017, **13**, 6131–6135.

S11 S. V. Sambasivarao and O. Acevedo, Development of OPLS-AA force field parameters for 68 unique ionic liquids, *J. Chem. Theory Comput.*, 2009, **5**, 1038–1050.

S12 D. Sezer, J. H. Freed and B. Roux, Parametrization, molecular dynamics simulation, and calculation of electron spin resonance spectra of a nitroxide spin label on a polyalanine α-helix, *J. Phys. Chem. B*, 2008, **112**, 5755–5767.

S13 W. Xiao, X. Wang, Q. Chen, T. Wu, Y. Wu, L. Dai and C. Song, A Novel and Green Method for the Synthesis of Ionic Liquids Using the Corresponding Acidic Ionic Liquid Precursors and Dialkyl Carbonate, *Chem. Lett.*, 2010, **39**, 1112–1113.

S14 U. Essmann, L. Perera, M. L. Berkowitz, T. Darden, H. Lee and L. G. Pedersen, A smooth particle mesh Ewald method, *J. Chem. Phys.*, 1995, **103**, 8577–8593.

S15 B. Hess, H. Bekker, H. J. C. Berendsen and J. G. E. M. Fraaije, LINCS: A linear constraint solver for molecular simulations, *J. Comput. Chem.*, 1997, **18**, 1463–1472.

S16 G. Bussi, D. Donadio and M. Parrinello, Canonical sampling through velocity rescaling, *J. Chem. Phys.*, 2007, **126**, 014101.

S17 L. M. Wang, V. Velikov and C. A. Angell, Direct determination of kinetic fragility indices of glassforming liquids by differential scanning calorimetry: Kinetic versus thermodynamic fragilities, *J. Chem. Phys.*, 2002, **117**, 10184–10192.

S18 T. Sato, G. Masuda and K. Takagi, Electrochemical properties of novel ionic liquids for electric double layer capacitor

applications, *Electrochim. Acta*, 2004, **49**, 3603–3611.
S19 Z. Bin Zhou, H. Matsumoto and K. Tatsumi, Structure and properties of new ionic liquids based on alkyl- and alkenyltrifluoroborates, *ChemPhysChem*, 2005, **6**, 1324–1332.
S20 A. Noda, K. Hayamizu and M. Watanabe, Pulsed-gradient spin-echo 1H and 19F NMR ionic diffusion coefficient, viscosity, and ionic conductivity of non-chloroaluminate room-temperature ionic liquids, *J. Phys. Chem. B*, 2001, **105**, 4603–4610.
S21 M. J. Earle, P. B. McCormac and K. R. Seddon, Regioselective alkylation in ionic liquids, *Chem. Commun.*, 1998, 2245–2246.
S22 T. Nishida, Y. Tashiro and M. Yamamoto, Physical and electrochemical properties of 1-alkyl-3-methylimidazolium tetrafluoroborate for electrolyte, *J. Fluor. Chem.*, 2003, **120**, 135–141.
S23 A. B. McEwen, Electrochemical Properties of Imidazolium Salt Electrolytes for Electrochemical Capacitor Applications, *J. Electrochem. Soc.*, 1999, **146**, 1687.
S24 J. D. Holbrey and K. R. Seddon, Tetrafluoroborates ; Ionic Liquids and Ionic Liquid Crystals, 1999, 2133–2139.
S25 J. G. Huddleston, A. E. Visser, W. M. Reichert, H. D. Willauer, G. A. Broker and R. D. Rogers, Characterization and comparison of hydrophilic and hydrophobic room temperature ionic liquids incorporating the imidazolium cation, *Green Chem.*, 2001, **3**, 156–164.
S26 W. Xu, L.-M. Wang, R. A. Nieman and C. A. Angell, Ionic Liquids of Chelated Orthoborates as Model Ionic Glassformers, *J. Phys. Chem. B*, 2003, **107**, 11749–11756.
S27 V. Strehmel, A. Laschewsky, H. Krudelt, H. Wetzel and E. Görnitz, Free Radical Polymerization of Methacrylates in Ionic Liquids, 2005, 17–36.
S28 J. M. Crosthwaite, M. J. Muldoon, J. K. Dixon, J. L. Anderson and J. F. Brennecke, Phase transition and decomposition temperatures, heat capacities and viscosities of pyridinium ionic liquids, *J. Chem. Thermodyn.*, 2005, **37**, 559–568.
S29 J. Dufour, L. Jorat, A. Bondeau, A. Siblini and G. Noyel, Shear viscosity and dielectric relaxanon time of dibutyl phthalate down to glass transition temperature., *J. Mol. Liq.*, 1994, **62**, 75–82.
S30 M. Y. M. Y. Ivanov, S. A. Prikhod’ko, N. Y. N. Y. Adonin, I. A. I. A. Kirilyuk, S. V. S. V. Adichtchev, N. V. N. V. Surovtsev, S. A. S. A. Dzuba, M. V. M. V. Fedin, S. A. Prikhod’Ko, N. Y. N. Y. Adonin, I. A. I. A. Kirilyuk, S. V. S. V. Adichtchev, N. V. N. V. Surovtsev, S. A. S. A. Dzuba and M. V. M. V. Fedin, Structural Anomalies in Ionic Liquids near the Glass Transition Revealed by Pulse EPR, *J. Phys. Chem. Lett.*, 2018, **9**, 4607–4612.
S31 S. A. Dzuba, Libration motion of guest spin probe molecules in organic glasses: CW EPR and electron spin echo study, *Spectrochim. Acta - Part A Mol. Biomol. Spectrosc.*, 2000, **56**, 227–234.
S32 N. P. Isaev and S. A. Dzuba, Fast Stochastic Librations and Slow Rotations of Spin Labeled Stearic Acids in a Model Phospholipid Bilayer at Cryogenic Temperatures, *J. Phys. Chem. B*, 2008, **112**, 13285–13291.
S33 S. S. Eaton and G. R. Eaton, in *eMagRes*, John Wiley & Sons, Ltd, Chichester, UK, 2016, vol. 5, pp. 1543–1556.